frontiers | Frontiers in Physics

TYPE Original Research
PUBLISHED 10 December 2025
DOI 10.3389/fphy.2025.1702903

OPEN ACCESS

EDITED BY
Imran Khan,
COMSATS Institute of Information Technology, Pakistan

REVIEWED BY
Xiujun Zhang,
Chengdu Neusoft University, China
Duc-Tan Tran,
Phenikaa University, Vietnam

*CORRESPONDENCE
Roosvel Soto-Diaz,
rosvel.soto@unismon.edu.co
Darius Andriukaitis,
darius.andrikatis@ktu.lt

RECEIVED 10 September 2025
REVISED 13 October 2025
ACCEPTED 24 October 2025
PUBLISHED 10 December 2025

CITATION
Nasimov R, Prauzek M, Konecny J, Abdelhaq M, Soto-Diaz R, Escorcia-Gutierrez J and Andriukaitis D (2025) Design and performance evaluation of orbital angular momentum metasurface for THz vortex waves generation based on fourier transform.
Front. Phys. 13:1702903.
doi: 10.3389/fphy.2025.1702903

Design and performance evaluation of orbital angular momentum metasurface for THz vortex waves generation based on fourier transform

Rashid Nasimov[1,2], Michal Prauzek[3], Jaromir Konecny[3], Maha Abdelhaq[4], Roosvel Soto-Diaz[5]*, José Escorcia-Gutierrez[6] and Darius Andriukaitis[7]*

[1]Department of Computer Engineering, Gachon University, Seongnam-si, Republic of Korea, [2]Department of Artificial intelligence, Tashkent State University of Economics, Tashkent, Uzbekistan, [3]Department of Cybernetics and Biomedical Engineering, VSB - Technical University of Ostrava, Ostrava-Poruba, Czechia, [4]Department of Information Technology, College of Computer and Information Sciences, Princess Nourah Bint Abdulrahman University, Riyadh, Saudi Arabia, [5]Biomedical Engineering Program, Universidad Simón Bolívar, Barranquilla, Colombia, [6]Department of Computational Science and Electronics, Universidad de la Costa, CUC, Barranquilla, Colombia, [7]Department of Electronics Engineering, Faculty of Electrical and Electronics Engineering, Kaunas University of Technology, Kaunas, Lithuania

Introduction: Because it is anticipated to be a new physical quantity for communication multiplexing and has significant potential for increasing channel capacity and enhancing spectrum resource utilization, researchers have been looking more closely at orbital angular momentum (OAM). Because of its potential to increase transmission capacity, vortex beams carrying orbital angular momentum (OAM) have recently become a focus of much investigation. One of the main challenges now is how to effectively manufacture OAM in the terahertz (THz) spectrum because existing THz vortex wave generation devices are constrained by only functioning at one frequency, having a small bandwidth, and having low conversion efficiency.

Methods: Therefore, this paper proposes a novel OAM metasurface design for generating vortex electromagnetic waves in the THz spectrum. The Pancharatnam-Berry phase idea and the phase superposition principle were used to create a single-layer reflective metasurface and a projected ultra-wideband reflective meta-atom.

Results and discussion: Each OAM mode in the reflected field was broken down using the Fourier transform, and the purity of the OAM modes was quantitatively examined. The dominant OAM mode had the highest energy weight share ($l = -2$) in all vortex waves at various frequencies, and the designed metasurface was further optimized to enhance the energy share corresponding to the dominant mode. With its high main mode energy, wide operating bandwidth, and excellent conversion efficiency, the proposed metasurface provides a benchmark for the effective production of wideband THz vortex waves.

KEYWORDS

metasurface, THz waves, orbital angular momentum, vortex beam generation, ultra-wideband metamaterial, dual-polarization

1 Introduction

Electrical waves with wavelengths between microwaves and infrared, ranging from 0.03 mm to 3 mm, and frequency between 0.3 THz and 10 THz are known as terahertz (THz) waves. Compared with microwaves, THz waves have narrower beams and have advantages such as large communication bandwidth, strong anti-interference ability, high resolution, and low photon energy. They also have the penetrability of millimeter waves and the controllability of light waves. It has a lot of potential applications in the domains of high-speed communications [1–3], bioimaging [4–6], holographic projection [7–9], and spectral detection [10–12]. Electromagnetic waves carry both linear and angular momentum; examples of angular momentum are orbital angular momentum (OAM) and spin angular momentum (SAM) [13, 14]. OAM, as a basic physical quantity of electromagnetic waves, was discovered and defined in Laguerre–Gaussian (LG) beams by [15] and has attracted widespread attention from researchers at home and abroad.

An essential aspect of electromagnetic waves is that their amplitude and polarization characteristics are the same as the OAM. They are all physical properties of electromagnetic waves. The beam carrying OAM is also called a vortex beam, and its phase distribution is $e^{-il\theta}$, characterized by a spiral phase wavefront. In theory, the spatial structures of OAM beams of different modes are different and mutually orthogonal. By utilizing their orthogonality, multiplexed orthogonal signals can be transmitted at the same frequency, greatly improving the spectrum efficiency and communication capacity of the communication system. Therefore, it has attracted widespread attention from researchers. High-speed wireless communications might benefit greatly from the combination of terahertz and orbital angular momentum technologies, which fully utilizes their respective advantages and can boost wireless communication systems' bandwidth and capacity. Therefore, generating reconfigurable high-quality OAM beams in the terahertz band is a prerequisite for the combination of terahertz and orbital angular momentum technologies.

Metasurfaces are thin-film devices composed of subwavelength structures that can obtain phase mutations on a two-dimensional plane at a subwavelength scale. They have low profiles, strong controllability, low losses, and are easy to process. These advantages make them one of the ideal methods for generating THz-OAM beams. Compared with natural materials, it has high flexibility and provides a new idea and method for the development of efficient wavefront control in the terahertz band. As of right now, scientists have finished a number of studies on THz wavefront control based on metasurfaces and investigated its many potential uses in vector beams, multiplexing, lenses, holography, etc. Considering the characteristics of different materials, periods and electromagnetic field distribution, the work of terahertz metasurface wavefront control can be divided into metal and dielectric metasurfaces, periodic, quasi-periodic and randomly distributed metasurfaces, and metasurface far-field and near-field wavefront control. These include the far-field and near-field wavefront control of THz, which differ greatly in concept, implementation technique, and application scenario due to the electromagnetic field dispersion characteristics. First, far-field wavefront control is the control of spatial light, and near-field control is mainly for bound states propagating on the surface, including surface waves or boundary states. There is an essential difference in the dispersion curves of the two. Secondly, the two also have great differences in processing methods and generation and detection means; in addition, there are also great differences in the application scenarios of far-field and near-field metasurface wavefront control. THz metasurfaces provide efficient solutions, such as high-resolution imaging and quick detection, because of their unique electromagnetic characteristics and microscale periodic structures. The drawbacks of conventional OAM sources in OAM production can be addressed by metasurfaces. It boosts the OAM generator performance by modifying electromagnetic waves, particularly in communication enhancement through increased bandwidth and conversion efficiency.

With a spiral spatial phase distribution exp (i$l\theta$) and a circular intensity distribution with a center of 0, the electromagnetic beam carrying OAM is also referred to as a vortex beam. The spatial azimuth is represented by θ, and the OAM topological charge number, or mode number, can be either an integer or a decimal. OAM is anticipated to become a new degree of freedom for transmission multiplexing and has a wide variety of applications in the disciplines of optics and communications since vortex waves with various modes are orthogonal and do not interfere with one another. Currently, the OAM has been successfully applied in the fields of optical micromanipulation [16], super-resolution imaging [17] and high-speed information transmission [18]. Therefore, how to efficiently generate THz vortex waves in broadband has become one of the key issues in related research fields.

Traditional methods of generating vortex waves include annular array antennas [19], spiral phase plates [20] and holographic diffraction gratings. Among them, the annular array antenna requires the design of a complex feeding network, which has high system costs. Other optical devices are large in size and expensive, which is not conducive to integration and miniaturization. In order to circumvent intricate feeding designs, metasurfaces [21, 22] are a revolutionary artificial structure made up of subwavelength components that can dynamically regulate electromagnetic waves' polarization, phase, and amplitude. Because of their

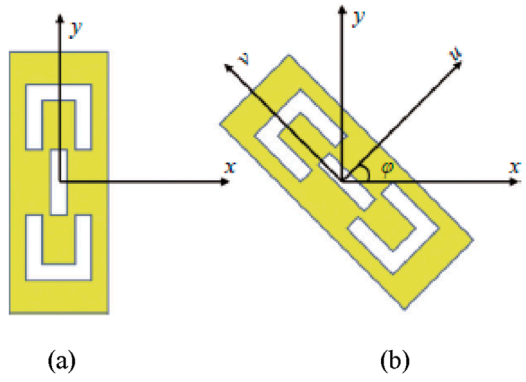

FIGURE 1
Metasruface unit design. **(a)** No rotation; **(b)** With rotation.

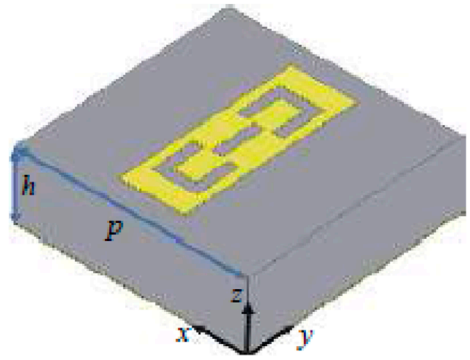

(a)

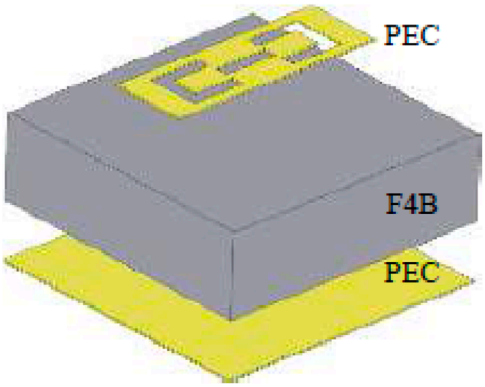

(b)

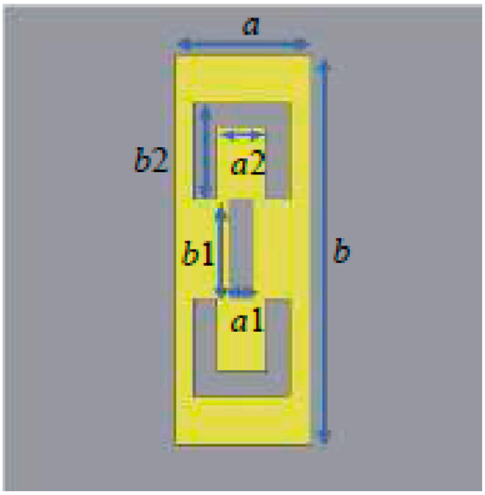

(c)

FIGURE 2
Anisotropic mestasurface unit design. **(a)** 3D side view; **(b)** Three-layer structure; **(c)** Unit structure.

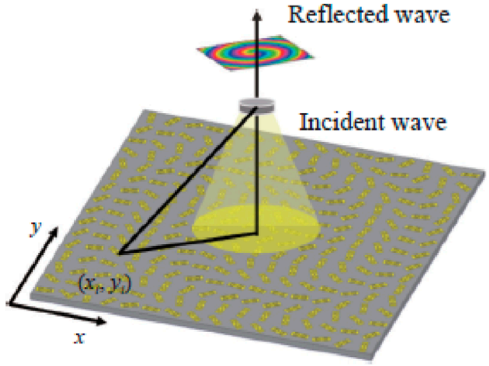

FIGURE 3
Vortex wave production principle by the metasurface.

compact size, light weight, low production cost, and ease of processing, researchers choose them. Terahertz vortex beams are now best produced using metasurfaces. In recent years, more and more researchers have tried to generate vortex waves through metasurfaces. For example, the authors in [23] proposed a metasurface with a "V" unit structure, which achieved the vortex wave generation with l = 1 in the infrared band. The authors in [24] used reconfigurable graphene loaded on the metasurface to generate vortex beams at 1.6 THz. Based on a multilayer graphene structure, the authors of [25] suggested a reflective metasurface that produced vortex beams with frequencies between 1.8 and 2.8 THz. In [26], the authors suggested a cross-structured unit metasurface that produced vortex beams with an 86% conversion efficiency in 0.8 THz ~ 1.4 THz. A frequency-switchable metasurface was proposed by the authors in [27], and it produced vortex beams at 0.7 THz and 1.23 THz, respectively. Vortex waves are produced in several modes. The above-mentioned metasurface has problems such as single working frequency, small bandwidth, and low conversion efficiency when generating terahertz vortex waves.

This paper proposes a broadband THz vortex wave metasurface composed of a single-layer geometric phase unit. The main innovations of this article are as follows.

1. The geometric phase is also called pancharatnam-berry (P-B) phase. The P-B phase is independent of frequency and is only related to the phase control related to the unit rotation angle, which realizes the high-efficiency generation of THz vortex waves.
2. By rotating the metasurface unit to obtain a reflection phase range of 0°–360°, a metasurface with $l = \pm 2$ is constructed according to the compensation phase distribution, and numerical simulation is performed on it.
3. The simulation results under circularly polarized plane wave excitation show that the ultra-broadband terahertz vortex wave metasurface proposed in this paper has the following advantages: a) Vortex waves are generated in a range of

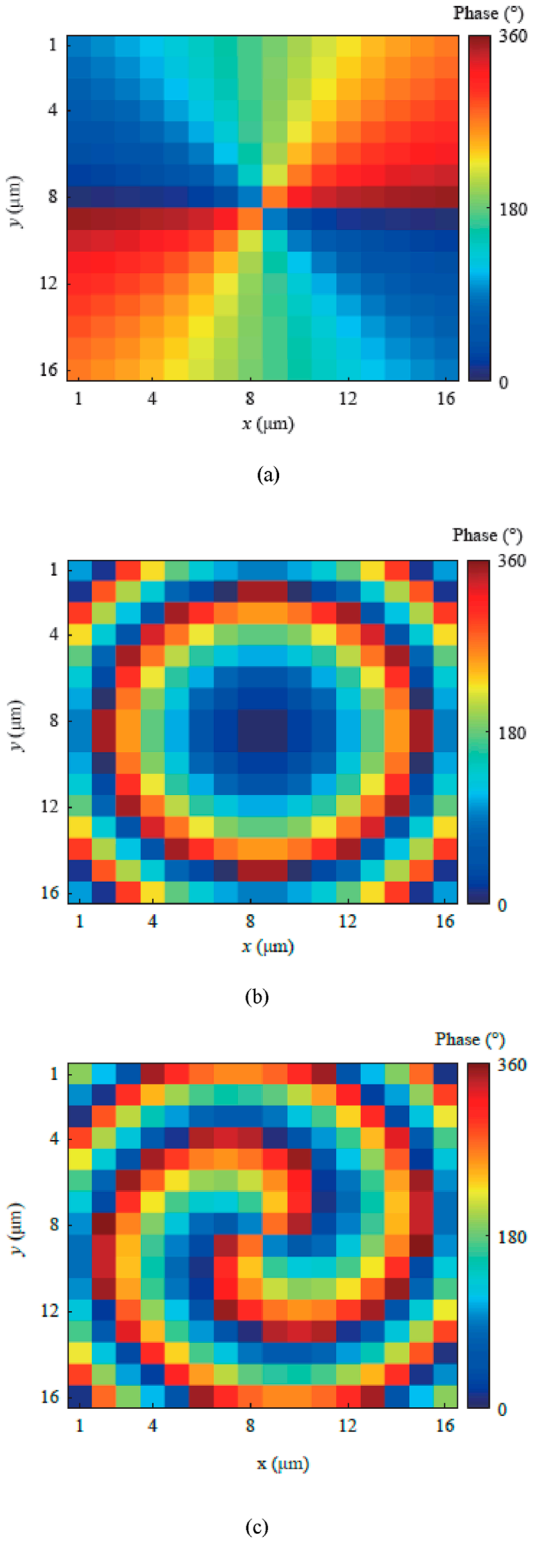

FIGURE 4
Phase distribution determination of metasurface. **(a)** Vortex phase φ_1; **(b)** focus phase φ_2; **(c)** total compensation phase φ_{tot}.

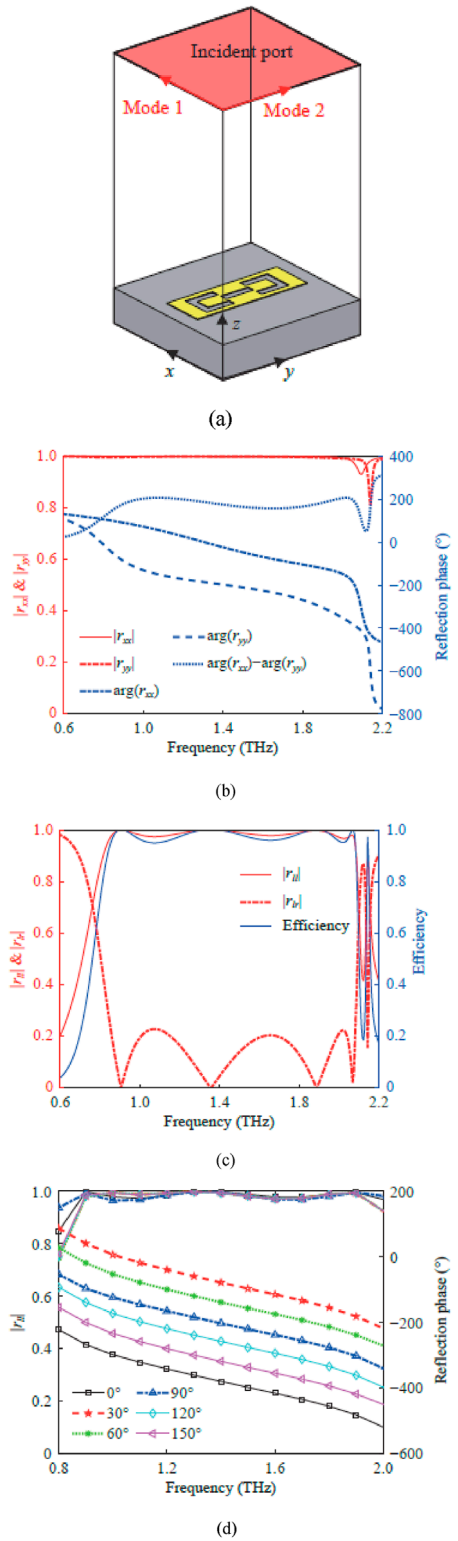

FIGURE 5
Simulation design and results. **(a)** Metasurface unit simulation setup; **(b)** Reflection spectrum and phase difference under linear polarization wave excitation; **(c)** Reflection spectrum and conversion efficiency under circularly polarized wave excitation; **(d)** Reflection spectra at different rotation angles under circular polarization wave excitation.

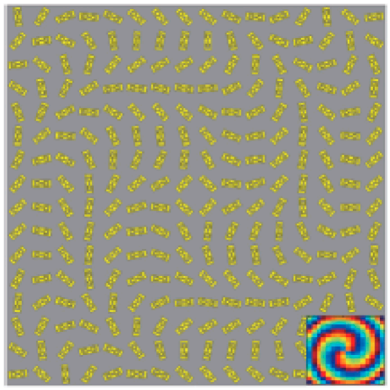

FIGURE 6
Metasurface topology with $l = \pm 2$ OAM mode.

0.82 THz to 2.09 THz (relative bandwidth 87.3%); b) The conversion efficiency of the metasurface is higher than 94.7%; c) The OAM mode purity is high, which provides a reference for efficient generation of THz vortex waves.

The remainder of this paper is organized as follows. In Section 2, the theoretical analysis and metasurface unit design is presented. In Section 3, the broadband vortex wave metasurface design is discussed. In Section 4, the simulations analysis is performed followed by performance comparison. In Section 5, the conclusion is discussed.

2 Theoretical analysis and metasurface unit design

The principle of the reflective metasurface to generate vortex beams is to reflect the plane wave with SAM into a structural wave carrying OAM. In order to simplify the design process and design high-performance units more conveniently, this study examines the metasurface's incident field and dispersed field using the Jones matrix. The conversion process of SAM-OAM under the incidence of circularly polarized waves is as follows, as seen in Figure 1, in the rectangular coordinate system, following the rotation of the metasurface unit by an angle φ.

$$r_{ll} = \frac{1}{2}\left\{\left(r_{xx} - r_{yy}\right) + j\left(r_{xy} + r_{yx}\right)\right\}e^{-j2\varphi} \tag{1}$$

$$r_{lr} = \frac{1}{2}\left\{\left(r_{xx} + r_{yy}\right) + j\left(r_{xy} - r_{yx}\right)\right\} \tag{2}$$

$$r_{rr} = \frac{1}{2}\left\{\left(r_{xx} - r_{yy}\right) - j\left(r_{xy} + r_{yx}\right)\right\}e^{j2\varphi} \tag{3}$$

$$r_{rl} = \frac{1}{2}\left\{\left(r_{xx} + r_{yy}\right) - j\left(r_{xy} - r_{yx}\right)\right\} \tag{4}$$

where, r_{xy}, r_{yx}, r_{lr} and r_{rl} denotes the reflection coefficients of cross-polarization; φ is the rotation angle; r_{ll} and r_{rr} are the reflection coefficients of co-polarization; r_{xx} and r_{yy} denotes the reflection coefficients of co-polarization for x- and y-polarized waves. It can be concluded from Equations 1–4 that when the circular polarization state of the reflected field remains unchanged relative to the incident field, the reflected field will carry an additional phase term $e^{-j2\varphi}$ and $e^{j2\varphi}$ related to the unit rotation angle φ. When the circular polarization state of the reflected field is converted, there will be no phase difference between the incident and scattered fields.

According to the P-B phase theory, any phase difference of 0°–360° can be obtained by rotating the metasurface unit, and the spiral phase wavefront can be modulated into a reflected wave, which is a necessary condition for the metasurface to generate a vortex beam [28]. The designed metasurface compensation phase surface is constructed using units with different rotation angles, which can realize any expected wavefront control of the reflected electromagnetic wave. Under circularly polarized wave incidence, in order to achieve a higher SAM-OAM conversion efficiency, the amplitude of the reflection coefficients r_{ll} and r_{rr} of the metasurface unit should be as close to 1 as possible. Therefore, to achieve efficient co-polarization conversion, the designed metasurface unit only needs to meet the following conditions:

$$\left|r_{xx}\right| \approx \left|r_{yy}\right| \approx 1 \tag{5}$$

$$\left|\arg\left\{r_{xx}\right\} - \arg\left\{r_{yy}\right\}\right| = 180^{\circ} \tag{6}$$

In order to achieve a larger system operating bandwidth and efficiently generate vortex beams in a wide bandwidth, Equation 7 states that the phase of the metasurface unit's co-polarization reflection coefficient at various rotation angles must have a similar slope within the ($f_{\min}$, $f_{\max}$) bandwidth.

$$\frac{\partial\Phi(l,l)}{\partial f_{\min}} \approx \frac{\partial\Phi(l,l)}{\partial f_i} \approx \frac{\partial\Phi(l,l)}{\partial f_{\max}} \tag{7}$$

Among them, $f_{\min}$ and $f_{\max}$ are the lower and upper cutoff frequencies; f_i is any frequency in the ($f_{\min}$, $f_{\max}$) band. $\Phi(l,l)$ represents the reflection phase under the incidence of left-hand circular polarization (LCP) waves. Applying right-hand circular polarization (RCP) wave incidence has the same effect.

Based on the above discussion, in order to achieve high-performance SAM-OAM conversion, Figure 2a illustrates the anisotropic metasurface unit designed in this paper. Figure 2b illustrates the unit's three-layer structure. The upper layer is a rectangular metal with a central opening and a "concave" groove that is symmetrical up and down. Polytetrafluoroethylene serves as the dielectric substrate in the middle layer. (F4B, $\varepsilon_r = 2.65$, $\tan\delta = 0.001$), with a height of $h = 30$ μm. The lower layer is a metal ground [29]. The unit is a mirror-symmetrical structure with a period of $p = 100$ μm. In order to achieve a larger bandwidth, the unit structure parameters are optimized by combining genetic algorithms, and finally a metasurface unit structure that meets the above theoretical requirements is obtained, as shown in Figure 2c. The specific parameters are $a = 28$ μm, $b = 80$ μm, $a1 = 5$ μm, $b1 = 20$ μm, $a2 = 10$ μm, $b2 = 20$ μm. By rotating the upper metal structure, the metasurface unit has a continuous reflection phase range of 0°–360°. The electrical size of the proposed metasurface unit is approximately 0.5 λ_0 (λ_0 is the center frequency wavelength) of the center frequency $f_c = 1.5$ THz.

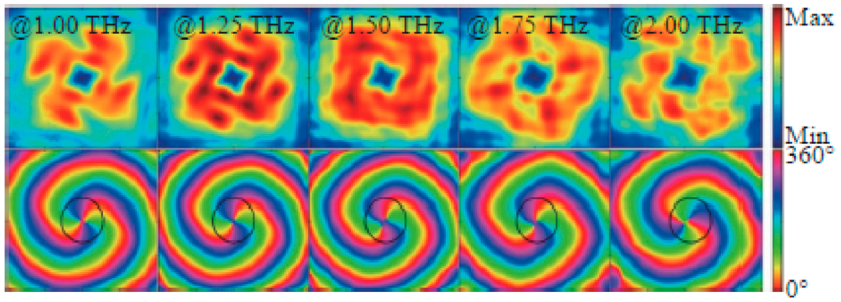

FIGURE 7
Amplitude and phase evaluation of vortex waves at $l = -2$ (near-field).

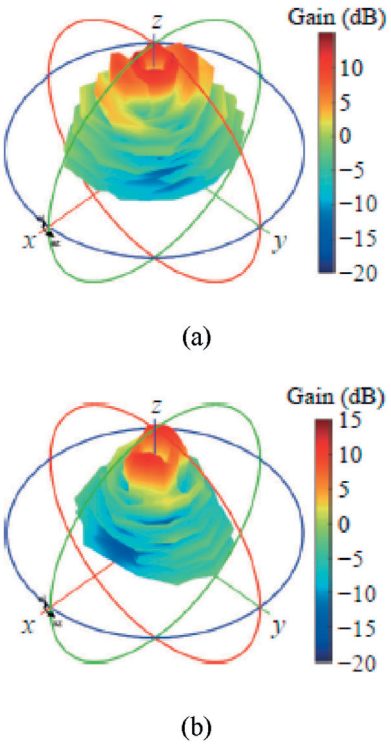

FIGURE 8
(Continued).

3 Broadband vortex wave metasurface design

Considering that 1.5 THz is the center frequency and it is composed of $M \times N$ units, $M = N = 16$ is selected in the design. The metasurface needs to have a vortex phase distribution so that the reflected wave can carry the vortex phase. Consequently, the phase distribution of $e^{il\theta}$ on the metasurface must be modulated in order to produce an OAM vortex beam in the metasurface reflection field [30]. Figure 3 illustrates how the metasurface generates vortex waves.

The metasurface is set on the x-*o*-y plane which is illustrated in Figure 3, and the position of any unit in the metasurface can be expressed by coordinates (x_i, y_i). The phase distribution of the vortex wave is defined in Equation 8:

$$\varphi_1(x_i, y_i) = l\tan^{-1}\left[\frac{y_i}{x_i}\right] \tag{8}$$

where, l is for phase singularity which indicates the OAM mode number [31–33]. This paper will take $l = \pm 2$ as an example to illustrate its principle, as shown in Figure 4a. The focusing phase must be combined in order to transform the spherical wave emitted by the feed antenna into a plane wave since it does not satisfy the plane wave incidence criterion of the vortex metasurface [34–36]. In this paper, the feed antenna is placed at the focus F, and its focusing phase distribution function is defined in Equation 9:

$$\varphi_2(x_i, y_i) = k_0\left\{\sqrt{F^2 + x_i^2 + y_i^2} - F\right\} \tag{9}$$

Where: $k_0(k_0 = 2\pi/\lambda_0)$ represents wave number in the free space; F represents the focal length. In this paper, it is set to F = 1,000 μm [37–39]. The focusing phase distribution is depicted in Figure 4b. Equation 10 can be used to determine the compensation phase needed for each metasurface unit at each place in accordance with the phase superposition principle.

$$\varphi_{tot}(x_i, y_i) = \varphi_1(x_i, y_i) + \varphi_2(x_i, y_i) \tag{10}$$

According to the compensation phase, the rotation angle of the unit at any position can be obtained as $\varphi_{tot}/2$. According to the numerical results displayed in Figure 4c, the reflected wave's phase distribution exhibits a spiral distribution and spans 0°–360° [40–42]. It is theoretically possible to create a continuous spatial phase change OAM vortex wave metasurface with an arbitrary topological charge number by determining the compensation phase and positioning the metasurface units with varying rotation angles.

4 Simulation results

4.1 Unit simulation results and analysis

We have given the structure and parameters of the metasurface unit above [43–45]. The simulation settings and simulation results

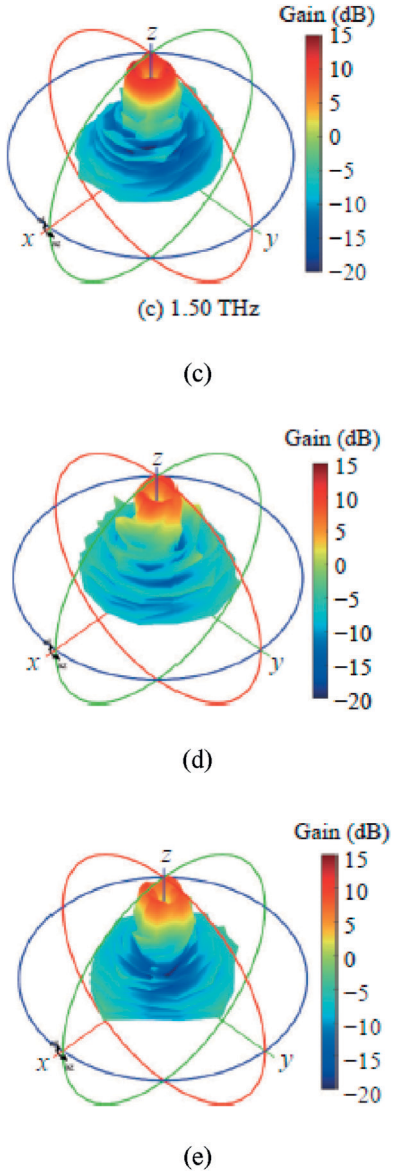

FIGURE 8
(Continued). 3D radiation pattern evaluation of vortex waves at $l = -2$(far-field). **(a)** 1 THz; **(b)** 1.25 THz; **(c)** 1.5 THz; **(d)** 1.75 THz; **(e)** 2 THz.

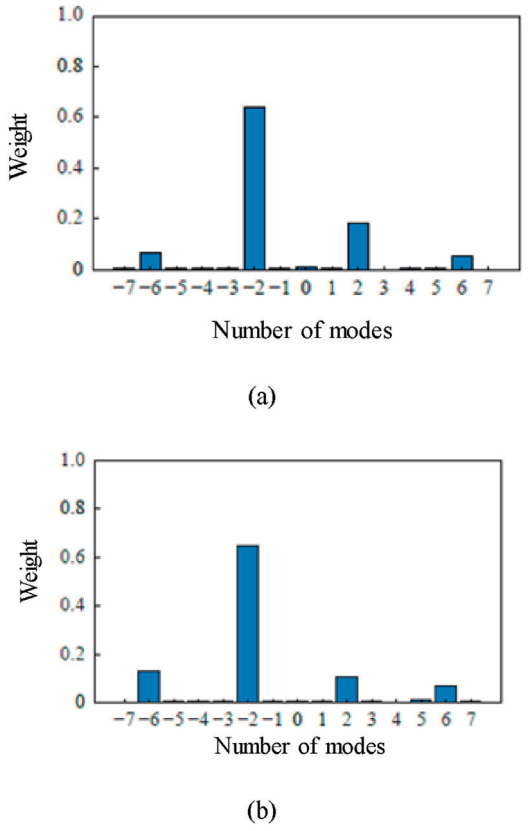

FIGURE 9
(Continued).

of the metasurface unit are illustrated in Figure 5a. We can see from Figure 5b, the amplitude of the reflection spectrum is close to 1 under the incidence of x- and y-polarized waves, satisfying Equation 5. It has a phase difference of 180° in a wide band, satisfying Equation 6. These two points are necessary conditions for generating vortex waves in a wide band [46–48]. Equation 11 can be used to determine the unit's conversion efficiency under the incidence of circularly polarized waves:

$$E_{\text{efficiency}} = \frac{r_{ll}^2}{\left(r_{ll}^2 + r_{lr}^2\right)} \tag{11}$$

As shown in Figure 5c, under circular polarization wave incidence, in 0.82 THz ~2.09 THz, the co-polarization reflection coefficient amplitude of the developed broadband unit is greater than 0.97 (relative bandwidth of 87.3%), a conversion efficiency greater than 94.7%, and a cross-polarization reflection coefficient amplitude less than 0.23 [49–51]. More importantly, it can be observed from Figure 5d that for the metasurface units at different rotation angles, the phase of their reflection spectra remains parallel within the bandwidth frequency range as expected, satisfying Equation 7, and the amplitude of the co-polarization reflection spectrum is greater than 0.95. These two points are very important for constructing a metasurface with high performance and high purity OAM characteristics.

The electromagnetic response simulation results of the metasurface unit above show that the metasurface unit proposed in this paper has high performance and can be used to construct an efficient broadband vortex wave metasurface [52–54].

4.2 Metasurface simulation results and discussion

According to the previously examined SAM-OAM conversion idea, the aforementioned metasurface units can be positioned at different rotational angles to construct a metasurface with the required vortex phase distribution $e^{(il\theta)}$. Figure 6 displays the metasurface with $l = \pm 2$ that was created in this paper [55–57]. Only

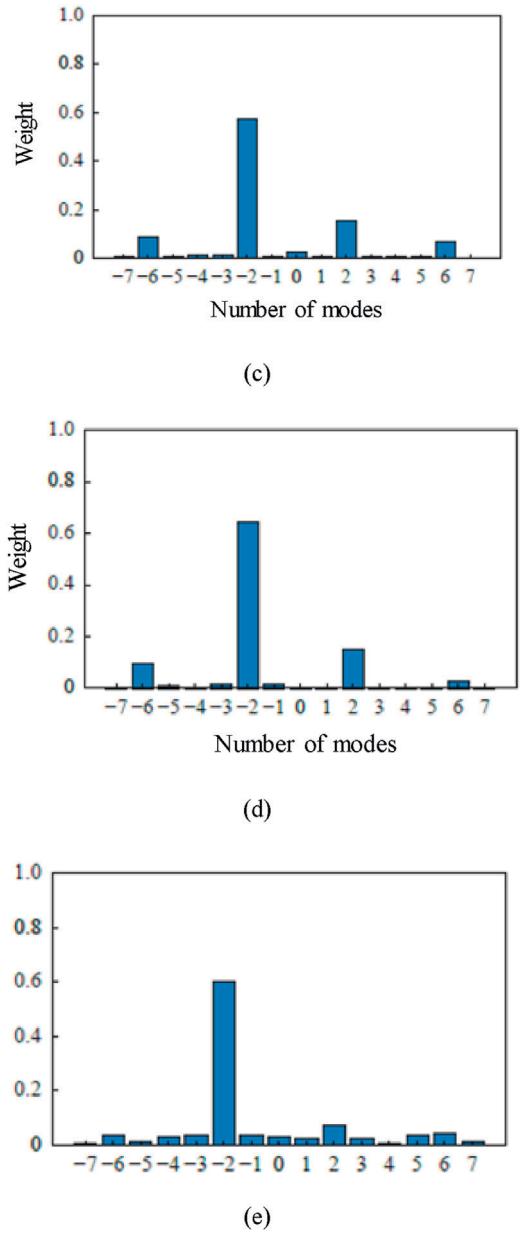

FIGURE 9
(Continued). Spectral weight of OAM under different frequencies. **(a)** 1 THz; **(b)** 1.25 THz; **(c)** 1.50 THz; **(d)** 1.75 THz; **(e)** 2 THz.

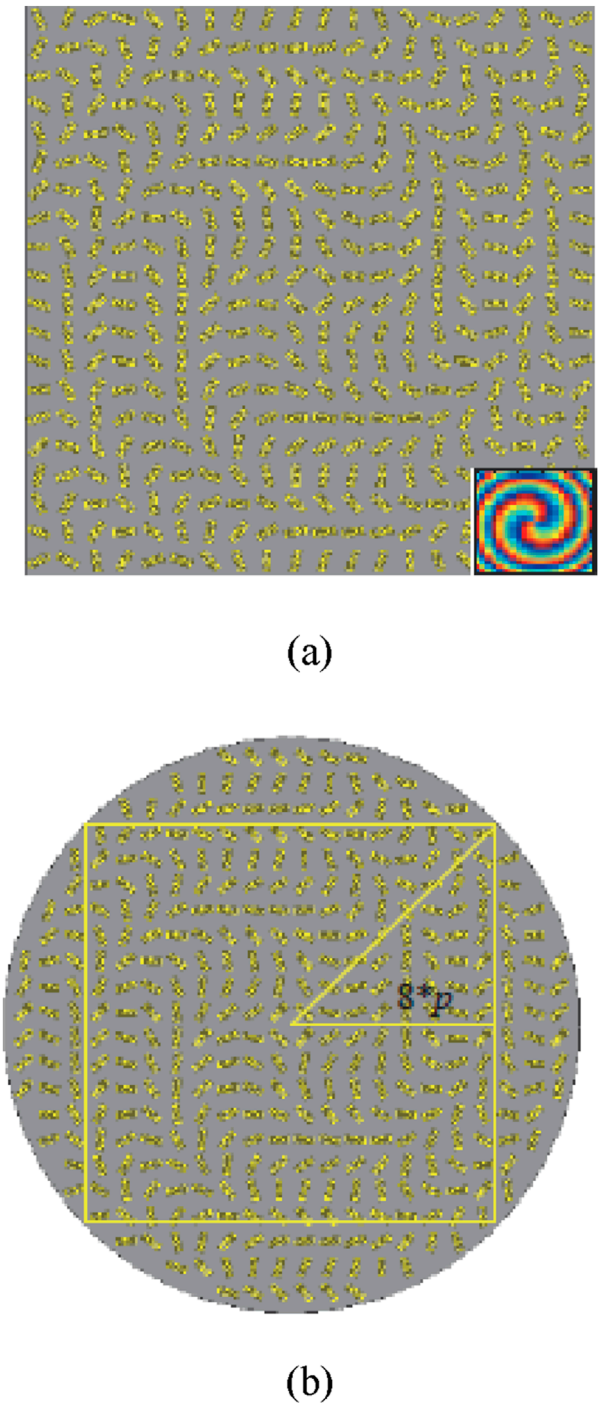

FIGURE 10
Optimized topology of metasurface with $l = \pm 2$ OAM mode. **(a)** Rectangular metasurface; **(b)** circular metasurface.

the incident wave's polarization direction is connected to the positive and negative values of l in Figure 6.

The specific topology is composed of 16 × 16 rotated metasurface unit arrays. The numerical simulation uses 1 THz to 2 THz to demonstrate that the suggested metasurface may produce vortex waves in a wideband, and its vortex characteristics are verified by near- and far-field performance. Under RCP wave, the metasurface proposed in this paper generates a THz wave with $l = -2$ [58–60]. The right-handed component in the reflected field at different frequencies is sampled and decomposed, and the sampling plane size is 1,600 μm × 1,600 μm, as shown in Figure 7. The electric field amplitude is a hollow ring, and the phase distribution is a symmetrical double helix around the unique point, as determined by the right-handed component in the sampling field. It is demonstrated that the metasurface created in this study can make the reflected electromagnetic wave convey OAM in a broadband since the phase change range is 0°~360°, which is consistent with attributes of OAM [61–63]. Figure 8 illustrates the 3D radiation pattern in the far-field of RCP in the

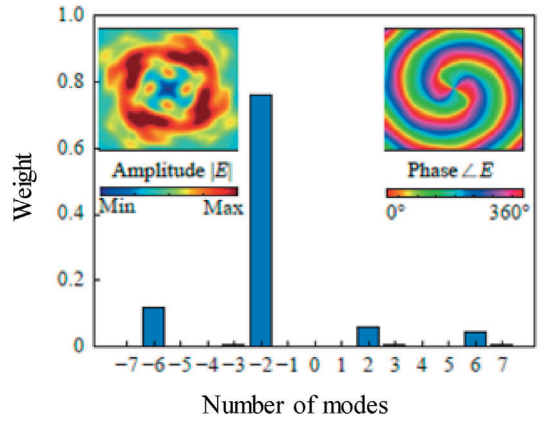

(a)

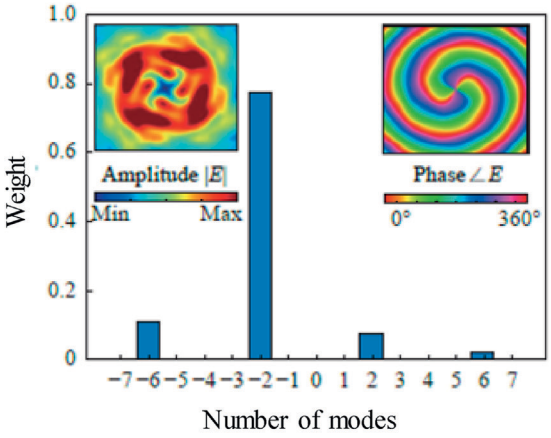

(b)

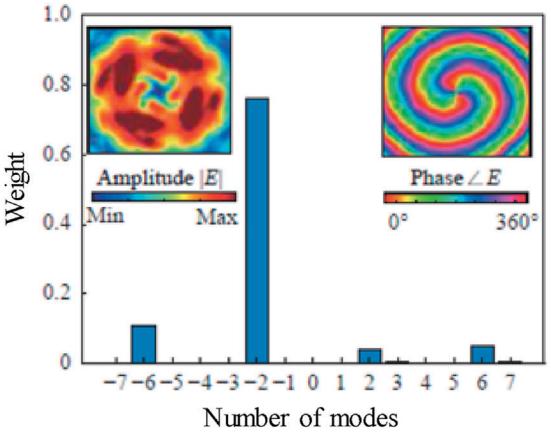

(c)

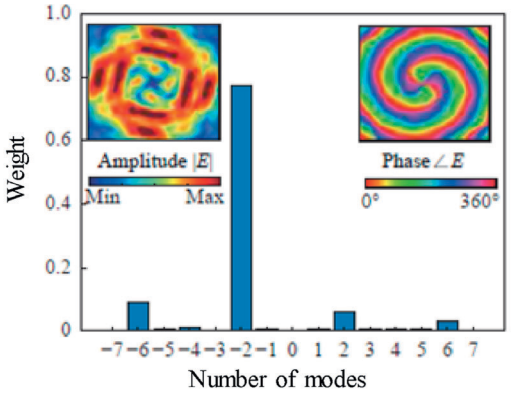

(d)

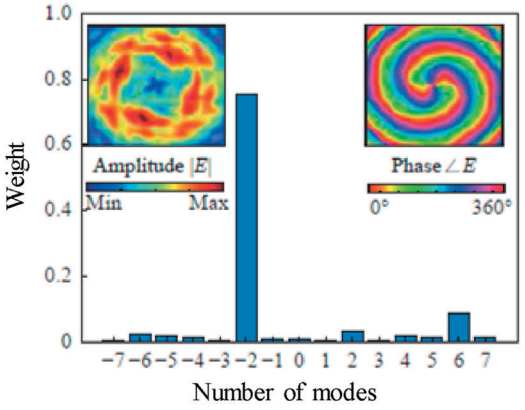

(e)

FIGURE 11
(Continued). Energy proportion and spectral analysis of the rectangular metasurface in near-field. **(a)** 1 THz; **(b)** 1.25 THz; **(c)** 1.50 THz; **(d)** 1.75 THz; **(e)** 2 THz.

reflected field excited by the Archimedean spiral antenna at several typical frequencies. The radiation gain at all frequencies is greater than 10 dB.

The OAM mode purity can be used to describe the energy distribution of vortex waves with different mode numbers in the reflection field, which can well illustrate the quality of vortex waves [64–66]. This work decomposes several OAM modes in the reflection field using the Fourier transform in order to quantitatively examine the OAM mode purity. Using the phase singularity of the vortex beam as the center, the Fourier transform is applied to a circular electric field data set along the main beam. The corresponding calculation formula is as follows in Equations 12, 13:

$$A_l = \frac{1}{2\pi}\int_0^{2\pi} E(\varphi)e^{-il\varphi}\mathrm{d}\varphi \tag{12}$$

$$E_{\text{energy weight}} = \frac{A_l}{\sum_{l'=-7}^{7} A_{l'}} \tag{13}$$

Among them, $E(\varphi)$ is the selected annular electric field; A_l is the amplitude of each mode. Considering the OAM mode of $l = -7$ to $l = 7$, the Fourier spectrum analysis are depicted in Figure 9. It can be seen from Figure 9, among the proportions of OAM modes at different frequencies, the main mode $l = -2$ has the highest

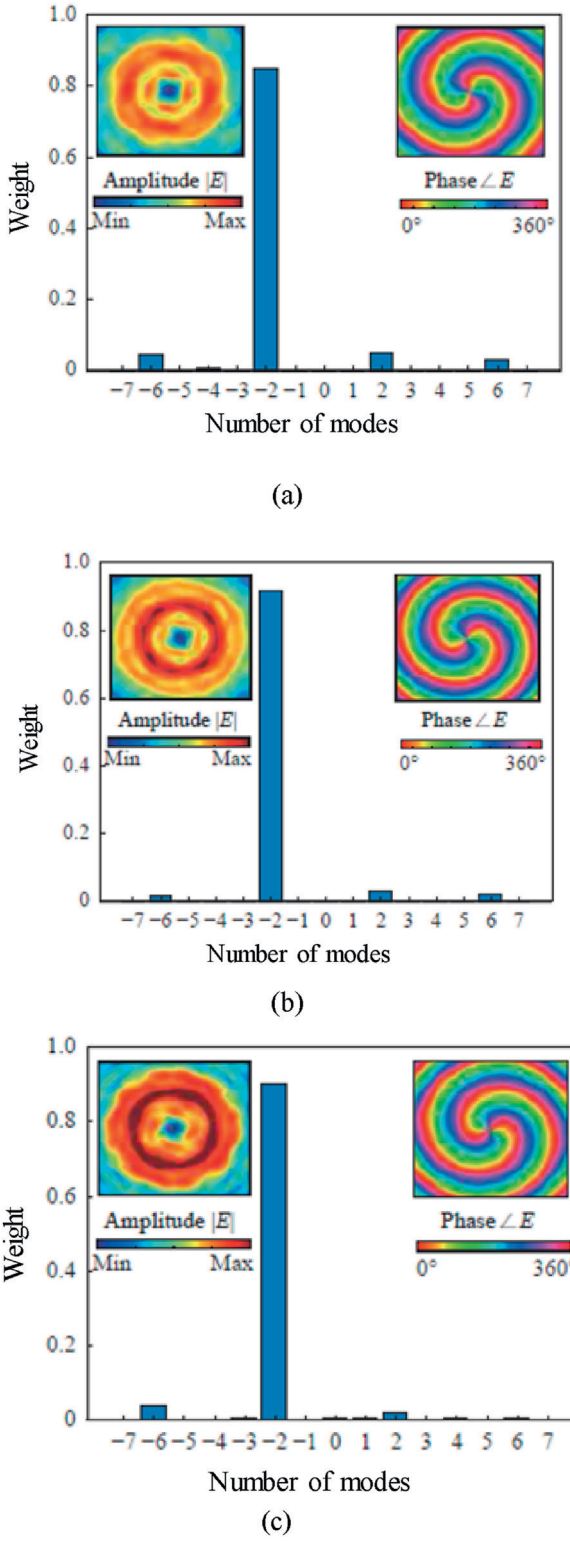

FIGURE 12
(Continued).

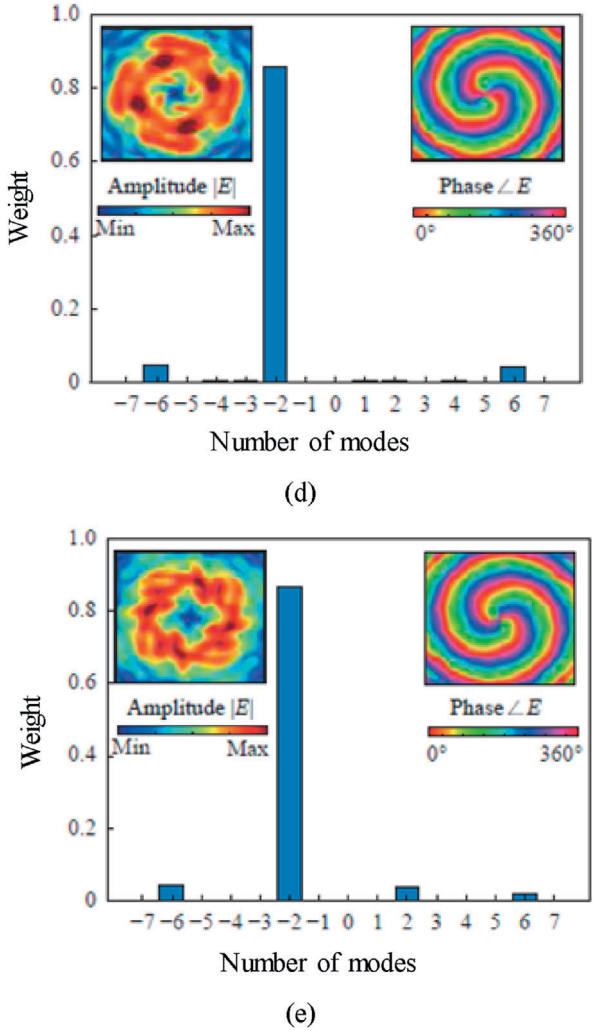

FIGURE 12
(Continued). Energy proportion and spectral analysis of the circular metasurface in near-field. **(a)** 1 THz; **(b)** 1.25 THz; **(c)** 1.50 THz; **(d)** 1.75 THz; **(e)** 2 THz.

energy [67–69], demonstrating that the primary mode of the vortex wave produced by the metasurface is identical to the mode that the metasurface specified.

4.3 Metasurface optimization simulation and discussion

In the above, we simulated the metasurface composed of 16×16 units and analyzed the mode intensity ratio. As shown in Figure 9, the intensity ratio of the main mode $l = -2$ is about 0.6 at each frequency. To improve the main mode intensity ratio, we first optimized the size of the metasurface, increased the number of units [70], and designed a rectangular metasurface composed of 20×20 metasurface units, as shown in Figure 10a. The vortex waves reflected by the rectangular metasurface at different frequencies and the corresponding spectra are shown in Figure 11.

As shown in Figure 11, the energy proportion of the main mode $l = -2$ at each frequency is about 0.76, which is significantly higher than that of the rectangular metasurface composed of 16×16 units. Rectangle is the most commonly used shape in metasurface design [71]. We optimized it to a circle to study its influence on the main mode intensity and designed a circular metasurface with a radius of

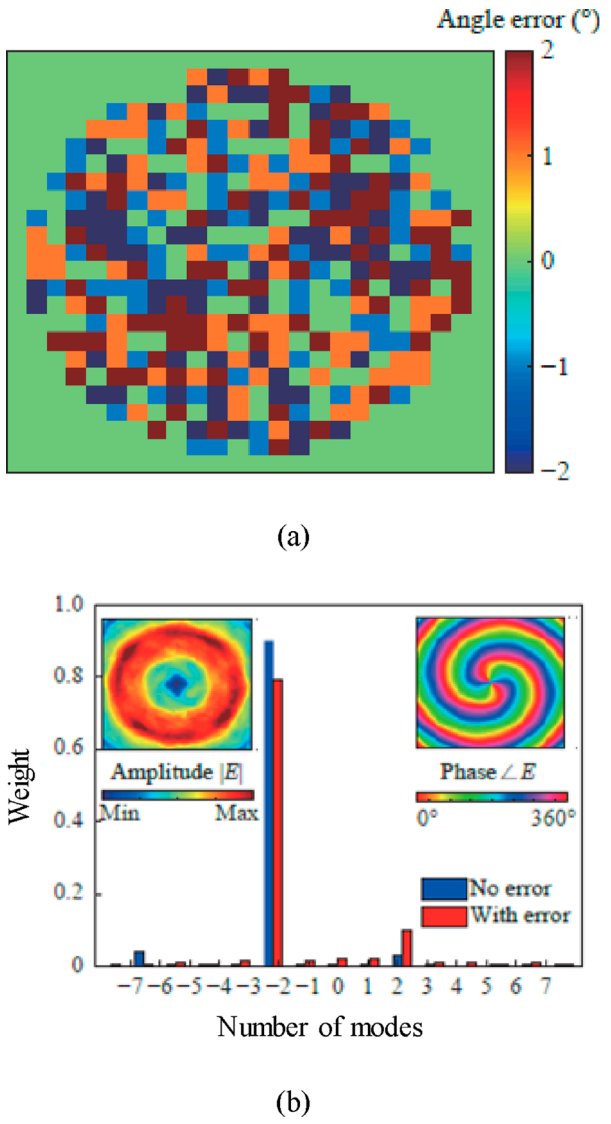

FIGURE 13
Vortex wave rotation angle error evaluation and spectral analysis. **(a)** Rotation angle error distribution; **(b)** Metasurface simulation results with errors (at 1.5 THz).

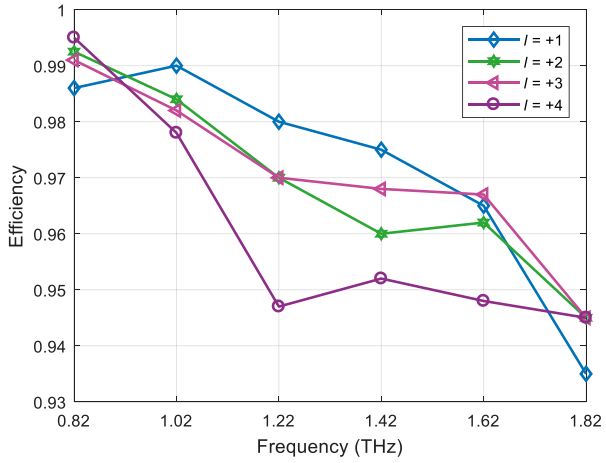

FIGURE 14
Efficiency evaluation of the metasurface.

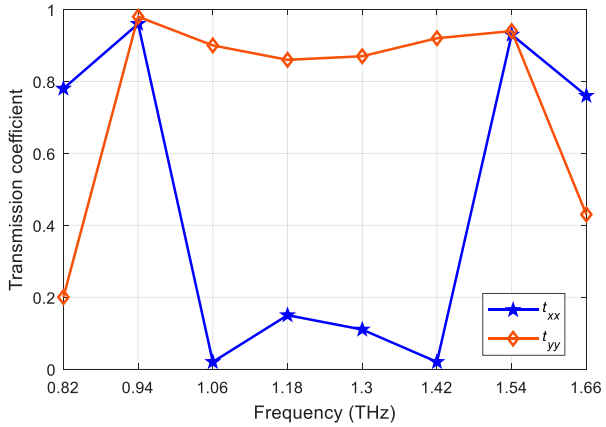

FIGURE 15
Transmission coefficient evaluation of the metasurface under various THz frequencies.

$8\sqrt{2} \times p$, as depicted in Figure 10b. Figure 12 shows the simulation results of the circular metasurface. As indicated in Figure 12, the intensity of $l = -2$ vortex wave reflected by the circular metasurface is increased to about 0.88 at each frequency, verifying that the circular metasurface design can effectively improve the main mode intensity.

The significance of simulation calculation is to provide reference for practice. In actual processing, errors are inevitable in metasurfaces. Therefore, this paper takes possible errors into consideration in simulation to study their influence on the mode field distribution of reflected vortex waves. The size error is randomly selected as ±2 μm, and the rotation angle error distribution is shown in Figure 13a. A circular metasurface is constructed and simulated at the center frequency, as illustrated in Figure 13b. Under the influence of the error, the main mode intensity is significantly reduced, and the intensity of other crosstalk modes is increased. However, on the whole, within a certain range, the primary mode intensity still makes up the majority of the mode field distribution of the reflected vortex wave, and the error has minimal impact on it.

Figure 14 evaluates the efficiency of the metasurface for different operating frequencies. As can be seen from Figure 14, the performance under different OAM modes is consistent with desired performance which validates the effectiveness.

Figure 15 evaluates the transmission coefficient of the metasurface with different values of THz frequencies. The x and y values of the transmission coefficient are analyzed. As can be seen from Figure 15, the transmission coefficient of both reached to maximum at 0.94 THz and 1.54 THz which is desired for practical deployment.

Table 1 shows the performance comparison of the unit designed by us and other units that generate OAM vortex wave beams in the THz band. The data used in Table 1 are all simulation data published in the corresponding articles. The results show that the unit designed

TABLE 1 Performance comparison of proposed and existing metasurface structures.

Reference	Operating frequency (THz)	Relative bandwidth (%)	Efficiency (%)	Phase modulation method
[25]	1.8 ~ 2.8	43.5	-	Graphene chemical potential
[26]	0.8 ~ 1.4	54.5	92	Geometric Phase
[27]	0.9 ~ 1.8	66.7	90	Geometric Phase
[28]	0.3 ~ 0.45	40	-	Geometric Phase
[29]	5.1 ~ 7.4	36.8	80	Transmission Phase
Proposed	0.82 ~ 2.09	87.3	94.7	Geometric Phase

by us can achieve efficient operation in a larger bandwidth and achieve a good balance between bandwidth and efficiency.

5 Conclusion

In this research, a high-performance geometric phase unit with free phase control of electromagnetic waves is proposed. To develop a broadband terahertz vortex wave metasurface with $l = \pm 2$, the geometric phase concept and the phase superposition principle are combined. The metasurface's near-field and far-field performances are simulated and confirmed. According to the simulation results, the developed metasurface can produce vortex beams carrying OAM in the 0.82 THz to 2.09 THz frequency range with the maximum energy share of the primary mode of OAM, a conversion efficiency of over 94.7%, and a radiation gain of over 10 dB. The designed metasurface is optimized and simulated. By increasing the number of units and designing the metasurface as a circle, the main mode intensity ratio can be effectively improved. The influence of errors on the mode field distribution of reflected vortex waves is simulated and analyzed. The benefits of the metasurface designed in this research include a large working bandwidth, high main mode intensity, high conversion efficiency, and a simple structure. It has the potential to be used in THz communication and imaging, and broadband terahertz vortex waves generation.

Data availability statement

The original contributions presented in the study are included in the article/supplementary material, further inquiries can be directed to the corresponding authors.

Author contributions

RN: Writing – original draft, Writing – review and editing. MP: Conceptualization, Data curation, Formal Analysis, Funding acquisition, Investigation, Methodology, Project administration, Resources, Software, Supervision, Validation, Visualization, Writing – original draft, Writing – review and editing. JK: Conceptualization, Data curation, Formal Analysis, Funding acquisition, Investigation, Methodology, Resources, Software, Supervision, Validation, Writing – original draft, Writing – review and editing. MA: Conceptualization, Data curation, Formal Analysis, Investigation, Methodology, Resources, Supervision, Validation, Visualization, Writing – original draft, Writing – review and editing. RS-D: Conceptualization, Data curation, Formal Analysis, Investigation, Methodology, Resources, Supervision, Validation, Writing – original draft, Writing – review and editing. JE-G: Conceptualization, Data curation, Formal Analysis, Investigation, Methodology, Project administration, Validation, Visualization, Writing – original draft, Writing – review and editing. DA: Conceptualization, Data curation, Formal Analysis, Investigation, Methodology, Project administration, Resources, Software, Validation, Writing – original draft, Writing – review and editing.

Funding

The author(s) declare that financial support was received for the research and/or publication of this article. This research was supported by Princess Nourah bint Abdulrahman University Researchers Supporting Project Number (PNURSP2025R97), Princess Nourah bint Abdulrahman University, Riyadh, Saudi Arabia. This article has been produced with the financial support of the European Union under the REFRESH – Research Excellence For REgion Sustainability and High-tech Industries project number CZ.10.03.01/00/22_003/0000048 via the Operational Programme Just Transition.

Conflict of interest

The authors declare that the research was conducted in the absence of any commercial or financial relationships that could be construed as a potential conflict of interest.

Generative AI statement

The author(s) declare that no Generative AI was used in the creation of this manuscript.

Any alternative text (alt text) provided alongside figures in this article has been generated by Frontiers with the support of artificial intelligence and reasonable efforts have been made to ensure accuracy, including review by the authors wherever possible. If you identify any issues, please contact us.

Publisher's note

References

1. Tian H, Shen H, Zhang X, Li X, Jiang WX, Cui TJ. Terahertz metasurfaces: toward multifunctional and programmable wave manipulation. *Front Phys* (2020) 8:584077. doi:10.3389/fphy.2020.584077

2. Hu D, He S, Li S, Zhu W. A dynamic beam switching metasurface based on angular mode-hipping effect. *Front Phys* (2024) 12:1–13. doi:10.3389/fphy.2024.1392115

3. Hou J, Zhang X, Guo Y, Zhang R, Guo M. Design of electromagnetic metasurface using two dimensional crystal nets. *Scientific Rep* (2023) 13(7248):7248. doi:10.1038/s41598-023-32660-y

4. Hoang T, Fusco V, Abbasi M, Yurduseven O. Single-pixel polarimetric direction of arrival estimation using programmable coding metasurface aperture. *Scientific Rep* (2021) 11:23830. doi:10.1038/s41598-021-03228-5

5. Qian C, Kaminer I, Chen H. A guidance to intelligent metamaterials and metamaterials intelligence. *Nat Commun* (2025) 16:1154. doi:10.1038/s41467-025-56122-3

6. Yildirim H, Storrer L, Doncker P, Louveaux J, Horlin F. A multi-antenna super-resolution passive Wi-Fi radar algorithm: combined model order selection and parameter estimatoin. *IET Radar, Sonar and Navigation* (2022) 16(8):1376–1387. doi:10.1049/rsn2.12267

7. Venneri F, Costanzo S, Borgia A. Fractal metasurfaces and antennas: an overview of advanced applications in wireless communications. *Appl Sci* (2024) 14(7):1–17. doi:10.3390/app14072843

8. Cai H, Gu L, Hu H, Zhan Q. Enhancement methods for chiral optical signals by tailoring optical fields and nanostructures. *Engineering* (2025) 45:25–43. doi:10.1016/j.eng.2024.12.022

9. Liu Z, Xu Y, Ji C. Fano-enhanced circular dichoism in deformable stereo metasurfaces. *Adv Mater* (2020) 32(8):1–14. doi:10.1002/adma.201907077

10. Zanotto L, Balisteri G, Rovere A, Kwon O, Morandotti R, Piccoli R. Terahertz scanless hypertemportal imaging. *Laser Photon Rev* (2023) 17(8):1–14. doi:10.1002/lpor.202200936

11. Wan M, Healy J, Sheridan J. Terahertz phase imaging and biomedical applications. *Opt and Laser Tech* (2020) 122:105859. doi:10.1016/j.optlastec.2019.105859

12. Wan Z, Gao Z, Gao F, Renzo MD, Alouini MS. Terahertz massive MIMO with holographic reconfigurable intelligent surfaces. *IEEE Trans Commun* (2021) 69(7):4732–4750. doi:10.1109/tcomm.2021.3064949

13. Lan F, Wang L, Zeng H, Liang S, Song T, Liu W, et al. Real-time programmable metasurface for terahertz multifunctional wave front engineering. *Light: Sci and Appl* (2023) 12(191):191. doi:10.1038/s41377-023-01228-w

14. Liu Y, Xu Y, Yu B, Liu W, Zhang Z, Cheng H, et al. Terahertz metasurfaces for polarization manipulation and detection: principles and emerging applications. *Adv Phys Res* (2025) 4(2):2400100. doi:10.1002/apxr.202400100

15. Wang Y, Bai L, Huang C, Xie J, Zhang D, Guo L. Orbital angular momentum of laguerre-gaussian beams with Non-zero radial index at limited aperture size. *Results Phys* (2023) 48(1):106436. doi:10.1016/j.rinp.2023.106436

16. Zhou M, Zhang W, Sun J, Chu F, Dong G, Nie M, et al. Atomic fabrication of 2D materials using electron beams inside an electron microscope. *Nanomaterials* (2024) 14(21):1718. doi:10.3390/nano14211718

17. Yang T, Shi H, Guo J, Qiao Z. Orbital-angular momentum-based super-resolution ISAR imaging for maneuvering targets: modeling and performance analysis. *Digital Signal Process.* (2021) 117:103197. doi:10.1016/j.dsp.2021.103197

18. Gong L, Zhang Q, Zhang H. Optical orbital angular momentum multiplexed data transmission under high scattering. *Light: Sci and Appl* (2019) 8(1):1–13. doi:10.1038/s41377-019-0140-3

19. Wu J, Huang Z, Ren X. Wideband millimeter-wave dual-mode dual circularly polarized OAM antenna using sequentially rotating feeding technique. *IEEE Antennas Wireless Propagation Lett* (2020) 19(8):1296–1300. doi:10.1109/LAWP.2020.2997057

20. Naseri H, Pourmohammadi P, Melouki N, Ahmed F, Iqbal A, Denidni T. Frequency-adjustable OAM antenna with co-divergent beams for IoT applications. *AEU – Int J Electron Commun* (2024) 177:155188. doi:10.1016/j.aeue.2024.155188

21. Wang C, Yang Y, Yang W, Wu J, Huang X, Jin J, et al. Wideband dual-mode vortex wave metasurface based on distance inversion method. *IEEE Trans Antennas Propagation* (2024) 72(12):9401–9410. doi:10.1109/tap.2024.3470229

22. Ye L, Su W, Hu K, Ding Z, Hu Z, Ren R, et al. Multi-functional switchable terahertz metasurface device prediction by K-nearest neighbor. *Chin J Phys* (2024) 91(1):734–742. doi:10.1016/j.cjph.2024.07.016

23. Schake M. Examining and explaining the generalized laws of reflection and refraction at metasurface gratings. *J Opt Soc America A* (2022) 39(8):1352–1359. doi:10.1364/josaa.460037

24. Ren Q, Wang L, Wang T, Wang S, Zhou Y, Kang L, et al. Terahertz vortex beam generation based on reflective and transmissive graphene metasurfaces. *Results Phys* (2024) 62:107846. doi:10.1016/j.rinp.2024.107846

25. Esfandiari M, Lalbakhsh A, Shehni P, Jarchi S. Recent and emerging applications of graphene-based metamaterials in electromagnetics. *Mater and Des* (2022) 221:1–13. doi:10.1016/j.matdes.2022.110920

26. Yang Q, Wang Y, Liang L, Yang M. Broadband transparent terahertz vortex beam generator based on thermally tunable geometric metasurface. *Opt Mater* (2021) 121:111574. doi:10.1016/j.optmat.2021.111574

27. Tokizane Y, Kristensen M, Ohno S, Degert J, Freysz E, Brasselet E, et al. Frequency-multiplexed terahertz multiple vortex beam generation. *Appl Phys Lett* (2025) 126:191106. doi:10.1063/5.0261433

28. He B, Liu J, Cheng Y, Chen F, Luo H, Li X. Broadband and thermally switchable reflective metasurface based on Z-shape InSb for terahertz vortex beam generation. *Physica E: Low-dimensional Syst nanostructures* (2022) 144:115373. doi:10.1016/j.physe.2022.115373

29. Li J, Zhang L. Simple terahertz vortex beam generator based on reflective metasurfaces. *Opt Express* (2020) 28(24):36403–36412. doi:10.1364/oe.410681

30. Niu L, Chen X, Lang Y, Xu Q, Zhang X, Ma J, et al. Metasurface-empowered high-efficiency and broadband terahertz vortex beam plates. *Appl Phys Lett* (2024) 124:081701. doi:10.1063/5.0183220

31. Ali SZ, Ahsan K, Khairi DU, Raza SA, Alhalabi W, Kazem LH, et al. Optimal dimensions and performance evaluation of a truncated spherical dielectric lens antenna at X-band frequencies. *PLoS ONE* (2025) 20(3):e0318547. doi:10.1371/journal.pone.0318547

32. Hwang D, Kim J, Yang J, Song HK. Intelligent-reflecting-surface-assisted multicasting with joint beamforming and phase adjustment. *Appl Sci* (2022) 13(1):386. doi:10.3390/app13010386

33. Hwang D, Nam SS, Yang J, Song HK. Beamforming for the successive relaying-based cooperative non-orthogonal multiple access transmission. *Appl Sci* (2024) 14(8):3246. doi:10.3390/app14083246

34. Yang X, Zhuang Y, Shi M, Sun X, Cao X, Zhou B. RatioVLP: ambient light noise evaluation and suppression in the visible light positioning system. *IEEE Trans Mobile Comput* (2024) 23(5):5755–5769. doi:10.1109/TMC.2023.3312550

35. Wang Y, Wang Y, Yu A, Hu M, Wang Q, Pang C, et al. Non-interleaved shared-aperture full-stokes metalens via prior-knowledge-driven inverse design. *Adv Mater* (2025) 37(8):2408978. doi:10.1002/adma.202408978

36. Zhou G, Huang J, Li H, Li Y, Jia G, Song N, et al. Multispectral camouflage and radiative cooling using dynamically tunable metasurface. *Opt Express* (2024) 32(7):12926–12940. doi:10.1364/OE.517889

37. Zhou S. Gwo-ga-xgboost-based model for radio-frequency power amplifier under different temperatures. *Expert Syst Appl* (2025) 278:127439. doi:10.1016/j.eswa.2025.127439

38. Sun J, Zhou S, Lin Q. A high-precision and fast modeling method for amplifiers. *Int J Numer Model Electron Networks, Devices Fields* (2025) 38(2):e70051. doi:10.1002/jnm.70051

39. Sun J, Zhou S. Cuckoo search-ExtraTrees model for Radio-frequency power amplifier under different temperatures. *Frequenz* (2025) 79(7-8):433–438. doi:10.1515/freq-2024-0298

40. Gan X. TianheGraph: topology-aware graph processing. *ACM Trans Archit Code Optim* (2025) 22:1–24. doi:10.1145/3750450

41. Gan X, Zhang Y, Wang R, Li T, Xiao T, Zeng R, et al. TianheGraph: customizing graph search for Graph500 on Tianhe supercomputer. *IEEE Trans Parallel Distributed Syst* (2022) 33(4):941–951. doi:10.1109/TPDS.2021.3100785

42. Zhang C, Zhang H, Dang S, Shihada B, Alouini M. Gradient compression and correlation driven federated learning for wireless traffic prediction. *IEEE Trans Cogn Commun Networking* (2025) 11(4):2246–2258. doi:10.1109/TCCN.2024.3524183

43. Zhang Y, Gang Y, Wu P, Fan G, Xu W, Ai B, et al. Integrated sensing, communication, and computation in SAGIN: joint beamforming and resource allocation. *IEEE Trans Cogn Commun Networking* (2025) 11:3128–3143. doi:10.1109/TCCN.2025.3577377

44. Wang Q, Li P, Zhang Y, Tan G, Yang Y, Rocca P. Robust design and tolerance analysis of shaped reflector antennas based on interval analysis. *IEEE Antennas Wireless Propagation Lett* (2025) 24(8):2392–2396. doi:10.1109/LAWP.2025.3564436

45. Ren Z, Yang Z, Mu W, Liu T, Liu X, Wang Q. Ultra-broadband perfect absorbers based on biomimetic metamaterials with dual coupling gradient resonators. *Adv Mater* (2025) 37(11):2416314. doi:10.1002/adma.202416314

46. Niu S, Liu X, Wang C, Mu W, Xu W, Wang Q. Breaking the trade-off between complexity and absorbing performance in metamaterials through intelligent design. *Small* (2025) 21(24):2502828. doi:10.1002/smll.202502828

47. Yang Y, Zhang Z, Zhou Y, Wang C, Zhu H. Design of a simultaneous information and power transfer system based on a modulating feature of magnetron. *IEEE Trans Microwave Theor Tech* (2023) 71(2):907–915. doi:10.1109/TMTT.2022.3205612

48. Bai X, Xiao Z, Shi H, Zhang K, Luo Z, Wu Y. Omnidirectional sound wave absorption based on the multi-oriented acoustic meta-materials. *Appl Acoust* (2025) 228:110344. doi:10.1016/j.apacoust.2024.110344

49. Guan Y, Yang L, Chen C, Wan R, Guo C, Wang P. Regulable crack patterns for the fabrication of high-performance transparent EMI shielding windows. *iScience* (2025) 28(1):111543. doi:10.1016/j.isci.2024.111543

50. Zhao Y, Xing S, Jin Q, Yang N, He Y, Zhang J. Excellent angular and electrical performance damage tolerance of wave-absorbing laminate via gradient A-T-A design. *Composites Commun* (2024) 46:101838. doi:10.1016/j.coco.2024.101838

51. Chen Y, Li H, Song Y, Zhu X. Recoding hybrid stochastic numbers for preventing bit width accumulation and fault tolerance. *IEEE Trans Circuits Syst Regular Pap* (2025) 72(3):1243–1255. doi:10.1109/TCSI.2024.3492054

52. Zhao Z, Chen X, Meng F, Yang Z, Liu B, Zhu N, et al. Design and analysis of a 22.6-to-73.9 GHz low-noise amplifier for 5G NR FR2 and NR-U multiband/multistandard communications. *IEEE J Solid-State Circuits* (2025) 60(9):3189–3201. doi:10.1109/JSSC.2025.3545463

53. Lu Z, Hao R, Wu D, Ding H, Chen L. An investigation of a self-powered low-frequency nonlinear vibration isolation system. *Eng Structures* (2024) 315:118395. doi:10.1016/j.engstruct.2024.118395

54. Li D, Li P, Zhao J, Liang J, Liu J, Liu G, et al. Ground-to-UAV sub-terahertz channel measurement and modeling. *Opt Express* (2024) 32(18):32482–32494. doi:10.1364/OE.534369

55. Wang G, Gao L, Huang G, Lei X, Cui C, Wang S, et al. A wavelength-stabilized and quasi-common-path heterodyne grating interferometer with sub-nanometer precision. *IEEE Trans Instrumentation Meas* (2024) 73:1–9. doi:10.1109/TIM.2024.3372212

56. Chang H, Feng S, Qiu X, Meng H, Guo G, He X, et al. Implementation of the toroidal absorption cell with multi-layer patterns by a single ring surface. *Opt Lett* (2020) 45(21):5897–5900. doi:10.1364/OL.404198

57. Wang F, Zhang S, Hong E, Quek TQS. Constellation as a service: tailored connectivity management in direct-satellite-to-device networks. *IEEE Commun Mag* (2025) 1–7. doi:10.1109/MCOM.001.2500138

58. Tian H, Wang J, Ma J, Li X, Zhang P, Li J. Improved energy-adaptive coupling for synchronization of neurons with nonlinear and memristive membranes. *Chaos, Solitons Fractals* (2025) 199:116863. doi:10.1016/j.chaos.2025.116863

59. Guan Y, Ding Y, Fang Y, Li J, Liu Y, Wang R, et al. Far-field femtosecond laser-driven λ/73 super-resolution fabrication of 2D van der Waals NbOI2 nanostructures in ambient air. *Nat Commun* (2025) 16(1):4149. doi:10.1038/s41467-025-59520-9

60. Deng J, Gao N, Chen X. Ultrawide attenuation bands in gradient metabeams with acoustic black hole pillars. *Thin-Walled Structures* (2023) 184:110459. doi:10.1016/j.tws.2022.110459

61. Deng J, Gao N. Broadband vibroacoustic reduction for a circular beam coupled with a curved acoustic black hole via nullspace method. *Int J Mech Sci* (2022) 233:107641. doi:10.1016/j.ijmecsci.2022.107641

62. Gao N, Huang Q, Pan G. Ultra-broadband sound absorption characteristics in underwater ultra-thin metamaterial with three layer bubbles. *Eng Rep* (2024) 6(11):e12939. doi:10.1002/eng2.12939

63. Cao Y, Ye F, Liang J, Qi L, Mo R, Huang B, et al. Structural-functional-integrated ultra-wideband microwave-absorbing composites based on in situ-grown graphene meta-nanointerface. *Adv Funct Mater* (2024) 34(52):2411271. doi:10.1002/adfm.202411271

64. Liang J, Ye F, Song Q, Cao Y, Xiao C, Qin Y, et al. Genetic algorithm designed multilayered Si3N4 nanowire membranes hybridized by dielectric wide-range tunable CVD graphene skin for broadband microwave absorption. *Composites B: Eng* (2025) 297:112298. doi:10.1016/j.compositesb.2025.112298

65. Zou X, Wang Y, Zong B, Xu X, Han L, Zhu H, et al. Miniaturized low-profile ultrawideband antipodal Vivaldi Antenna Array loaded with edge techniques. *IEEE Trans Antennas Propagation* (2025) 1:1. doi:10.1109/TAP.2025.3606193

66. Meng Z, Shen F, Gazor S. WLB-CANUN: widely linear beamforming in coprime array with non-uniform noise. *IEEE Trans Vehicular Tech* (2025) 74(4):5833–5842. doi:10.1109/TVT.2024.3504278

67. Yin R, Peng J, Cai Y, Wu C, Champagne B, Al-Dhahir N. Radar-assisted predictive beamforming for UAV-aided networks: a deep-learning solution. *IEEE Trans Vehicular Tech* (2025) 74:16079–16093. doi:10.1109/TVT.2025.3572037

68. Yin R, Shi Y, Qi W, Wu C, Wang W, Huang C. Joint beamforming and frame structure design for ISAC networks under imperfect synchronization. *IEEE Trans Cogn Commun Networking* (2025) 11(4):2259–2274. doi:10.1109/TCCN.2024.3510542

69. Xu H, Wei H, Chen H, Chen Z, Zhou X, Xu H, et al. Effect of periodic phase modulation on the matched filtering with insufficient phase-shift capability. *IEEE Trans Aerospace Electron Syst* (2025) 61(3):5755–5770. doi:10.1109/TAES.2024.3520959

70. Xu H, Zhang Y, Chen Z, Pan Q, Quan Y. An optimization-based deconvolution approach for recovering time-varying phase modulation signal of metasurface. *IEEE Trans Antennas Propagation* (2025) 73(8):5993–6007. doi:10.1109/TAP.2025.3567818

71. Fan S, Han C, He K, Bai L, Chen L, Shi H, et al. Acoustic moiré flat bands in twisted heterobilayer metasurface. *Adv Mater* (2025) 37(29):2418839. doi:10.1002/adma.202418839